Negative apparent chargeability in time-domain induced polarisation data

Dahlin, Torleif; Loke, Meng Heng

Published in:
Journal of Applied Geophysics

DOI:
10.1016/j.jappgeo.2015.08.012

2015

Journal of Applied Geophysics 123 (2015) 322–332

Contents lists available at ScienceDirect

Journal of Applied Geophysics

journal homepage: www.elsevier.com/locate/jappgeo

Negative apparent chargeability in time-domain induced polarisation data

T. Dahlin [a,*], M.H. Loke [b]

[a] Engineeering Geology, Lund University, Box 118, Lund SE-22100, Sweden
[b] Geotomo Software, 115 Cangkat Minden Jalan 6, Gelugor, Penang 11700, Malaysia

ARTICLE INFO

Article history:
Received 28 April 2015
Received in revised form 20 August 2015
Accepted 28 August 2015
Available online 4 September 2015

Keywords:
Time-domain
Induced polarisation
TDIP
Negative
Chargeability

ABSTRACT

It appears to be relatively common to assume that negative apparent chargeability data in time-domain induced polarisation (IP) surveying is a sign of bad data quality. Negative IP data can however occur as a consequence of the distribution of chargeable zones in the ground, which is well documented in literature. A general mechanism behind negative IP data is proposed as follows; if the chargeable zones are mainly located in zones of negative sensitivity, and there is low or no chargeability in the positive sensitivity volumes in the investigated volume, it will result in negative apparent chargeability.

Numerical modelling confirms that the phenomenon will typically occur for longer electrode separation if the chargeability is concentrated in a thin layer at the surface only, but that other distributions of the chargeable bodies can also cause negative IP data. Different electrode arrays differ in tendency to produce negative IP data, where dipole–dipole and pole–dipole arrays are more prone to generate negative data than nested arrays in the modelled examples. In addition to the relative location of the chargeable zone the resistivity is important for its impact on the apparent chargeability.

Field data recorded in connection with the 3rd International IP Workshop on Ile d'Oléron in April 2014 confirm that negative apparent chargeability can be caused by a thin chargeable layer at the surface. The abundant negative IP data can be explained by an inverted model with low residuals, in which the chargeability is concentrated in a thin layer with modest chargeability close to the surface. Removing the data with negative apparent chargeability before inversion results in apparently poor resolution of the bottom layer and artefacts that are not present in the inversion results from the original data set. The results clearly demonstrate that negative apparent chargeability data can be a result of the distribution of chargeable zones in relation to the sensitivity distribution, and that such data should not be edited away on a routine basis since they contain important information.

1. Introduction

Earth resistivity tomography (ERT) has become widely used for engineering and environmental applications in the last couple of decades thanks to the relatively fast and simple field procedure in combination with availability of easy to use inversion software (Auken et al., 2006; Dahlin, 2001; Loke et al., 2014). Many modern ERT instruments can measure time-domain induced polarisation (TDIP), and it has been shown that IP can significantly enhance the information for environmental and engineering applications (e.g. Dahlin et al., 2010; Gazoty et al., 2012; Leroux et al., 2007). However, measurement of resistivity is very robust from a data quality point of view, whereas IP data acquisition is much more sensitive to noise contamination of the data due to smaller signal levels in combination with shorter delays and integration times (Dahlin and Leroux, 2012). This is particularly critical if the IP data is intended for extraction of spectral information, which is a way ahead for enhancing the information content that can be extracted from TDIP data (Fiandaca et al., 2012, 2013; Hönig and Tezkan, 2007).

In order to develop robust routines for data quality assessment of TDIP data it is essential to have a physically based understanding of possible IP responses. In DC resistivity surveying negative data are generally a sign of measurement technical problem unless the electrode layout geometry is such that the geometrical factor is negative, although there can be exceptions to this due to 3D geological structures (Jung et al., 2009). It appears to be a common belief that the same applies to induced polarisation (IP) measured in time domain, at least within the near surface geophysics community, and that negative IP data are a sign of data quality problems. It is thus not uncommon to edit away all negative IP data as part of a data processing routine, but this can lead to loss of important information as explained below.

It is well documented that negative IP data can occur as a result of a shallow chargeable zone or layer (Bertin, 1976; Loeb, 1976; Sumner, 1976), and it was understood that it could be caused by a simple

* Corresponding author.
E-mail address: torleif.dahlin@tg.lth.se (T. Dahlin).

http://dx.doi.org/10.1016/j.jappgeo.2015.08.012
0926-9851/

geometric effect (Loeb, 1976). The mineral prospection IP community is probably aware of this, and Ranieri et al. (1996) have presented such results from a hydrogeological survey. Dieter et al. (1969) presented numerical modelling results for 1D soundings over spheres and ellipsoids that demonstrated that negative apparent chargeability can occur around such laterally limited bodies. Nabighian and Elliot (1976) studied 1D soundings over horizontally layered structures, and presented an analytical solution for the three layer case. They concluded that negative IP effects can be obtained whenever polarizable layers are overlying resistivity sequences of type K ($\rho_1 < \rho_2 > \rho_3$) and type Q ($\rho_1 > \rho_2 > \rho_3$).

We present a generally applicable way of explaining negative apparent chargeability caused by the geometric distribution of chargeable zones based on the sensitivity function, with the aim to provide an easier way to understand why and under which circumstances it can occur in complex geometries with 2D as well as 3D variation in the ground properties. Numerical modelling examples and a field example are used for demonstration. The forward and inverse modelling is limited to the integral chargeability, whereas modelling of full decay curves is left to future studies.

2. Sensitivity distribution and negative IP data

2.1. Resistivity sensitivity distribution

The sensitivity distribution determines how different parts of the ground contribute to the measured apparent resistivity of a particular four electrode array. The sensitivity distribution of vertical cross sections through the 3D sensitivity distribution for some common electrode arrays is shown in Fig. 1. The relative contribution of different parts of the ground is weighted with the magnitude of the sensitivity function, so that higher values of the sensitivity function gives a higher influence on the measured value. The sensitivity is given by the Fréchet derivative which can be calculated analytically for homogeneous ground (McGillivray and Oldenburg, 1990). The sensitivity distributions are different for inhomogeneous ground and have to be estimated by numerical modelling.

It can be noticed that the sensitivities are much higher at the surface close to the electrodes than at larger depths (Fig. 1). This means that near surface variation will have a major impact on the measured values, and that this must be accounted for carefully in the interpretation of the data in order to recover the more subtle contributions from deeper strata. Furthermore it can be noted that there are major zones of negative sensitivity, for example in between the C and P electrodes for the nested arrays (Fig. 1a–d) and between the C and P dipoles for the dipole–dipole array (Fig. 1e–f). The negative sensitivity leads to effects that can be counter intuitive, e.g. in otherwise homogeneous ground insertion of a high resistive block in a zone with negative sensitivity would lead to a smaller measured apparent resistivity.

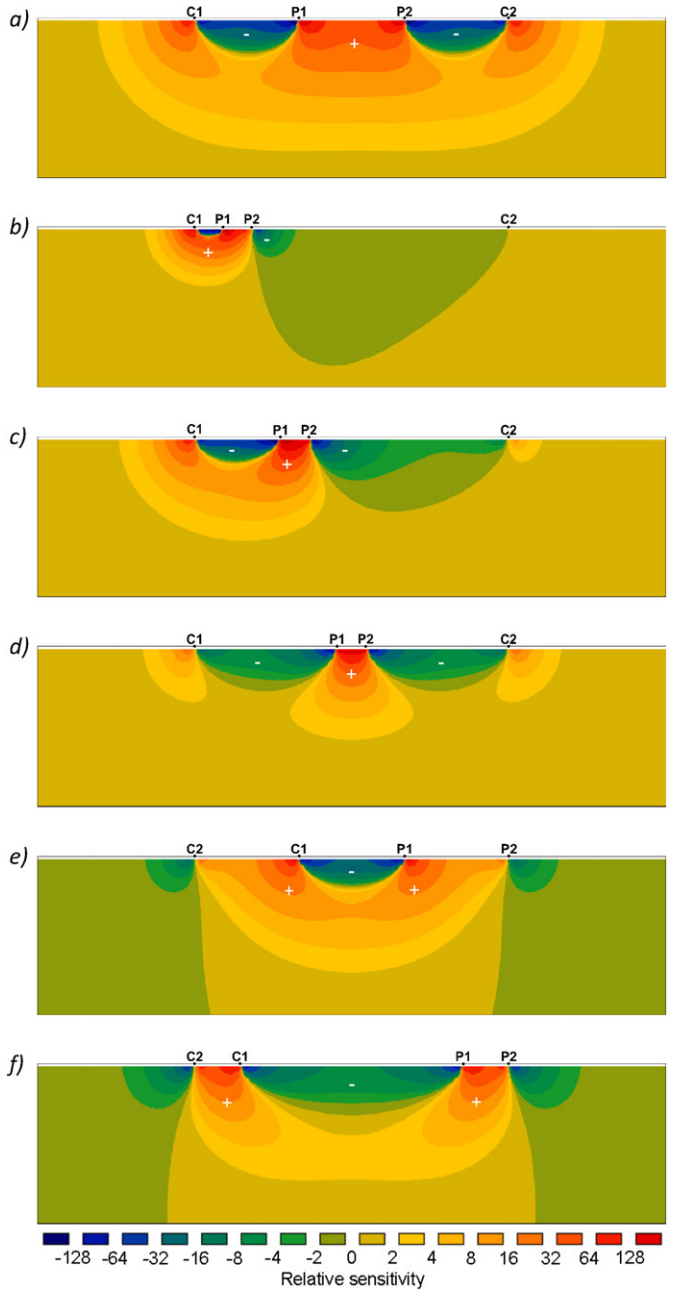

Fig. 1. Sensitivity distribution for; a) Wenner array, b) multiple gradient array (s = 9, n = 1), c) multiple gradient array (s = 9, n = 3), d) multiple gradient array (s = 9, n = 5), e) dipole–dipole array (n = 1), and f) dipole–dipole array (n = 5).

2.2. Sensitivity distribution and IP effect

The sensitivity distribution will have consequences for the possible occurrence of negative apparent chargeability. To illustrate the mathematical relationship between the apparent IP values and the model resistivity sensitivity, we use the theoretical formulation by Seigel (1959). The apparent IP value (M_a) is given by a summation of the intrinsic IP (m) of all the regions of the subsurface.

$$M_a = \sum_{j=1}^{n} B_j m_j$$

where the model has n discrete regions. The coefficient B_j is given by

$$B_j = \frac{\rho_j}{\rho_a}\frac{\partial \rho_a}{\partial \rho_j}$$

where ρ_a is the apparent resistivity and ρ_j is the model resistivity. In a region of the subsurface where the partial derivative term is negative, the contribution of that region to the apparent IP value is also negative. We note that the partial derivative $\frac{\partial \rho_a}{\partial \rho_j}$ is basically the integral of the Frechet derivative (sensitivity) over the volume of the jth region of the subsurface. The Frechet derivative is independent of the resistivity for a homogenous medium. However, it is dependent on the resistivity distribution for a non-homogenous medium. Nabighian and Elliot (1976) derived the equations for the B_j terms for a 1-D layered earth model. For general 2-D and 3-D models, the partial derivative values can be calculated numerically using the adjoint-equation method (McGillivray and Oldenburg, 1990).

Consider a chargeability distribution with a thin chargeable top layer overlying a layer with no detectable chargeability, as illustrated by the

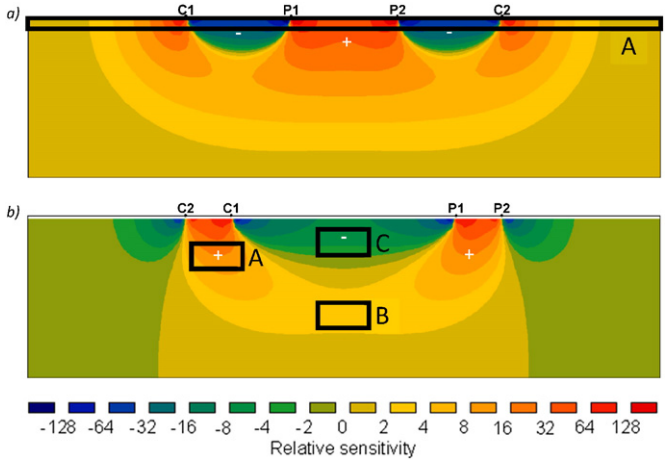

Fig. 2. Sensitivity distribution with location of chargeable bodies indicated for; a) Wenner array, b) dipole–dipole array with n-factor 5.

indicated zone A in Fig. 2a. The sensitivity distribution for longer electrode separations in this case have major zones of negative sensitivity near the surface where the chargeable zone is located, and positive sensitivity zones in the deeper parts. This means that when transmitted current is turned off all contribution to the measured signal for the deeper parts where positive sensitivity dominates disappears immediately, whereas the chargeable near surface zone produces a negative potential that decays according to its IP properties.

In case of dipole–dipole array a chargeable zone between the current electrodes where the sensitivity is positive, in an otherwise non-chargeable environment, will give positive apparent chargeability as illustrated by zone A in Fig. 2b. The same applies to a chargeable zone in between the potential electrodes or at depth as indicated by zone B. If on the other hand the only chargeable zone is located in between the current and potential dipoles, zone C in Fig. 2b, it will produce a negative residual potential after current has been turned off and the signal contributions from positive contribution volumes are gone.

2.3. Other possible causes of negative IP effect

Other possible sources of negative IP data include inductive and capacitive coupling. Inductive coupling would only occur for very early decay times and should thus be possible to separate from the slower IP decays, although precise limits for this do not exist but would require complicated numerical modelling for each individual case. Capacitive coupling can be a severe problem, especially in cases with high contact resistances between electrodes and ground. Large and unrealistic negative as well as positive IP responses can be caused by capacitive coupling, and it can be expected that less extreme decay curves that can be mistaken for actual IP decays can arise as well. Capacitive coupling problems can be reduced by measuring with separated electrode cable spreads for current transmission and potential measurement (Dahlin and Leroux, 2012).

Intrinsic negative chargeability has been reported for soft clays by Brandes and Acworth (2003). That is beyond the scope of this paper, but it further underlines that negative apparent chargeability data should not be dismissed by default.

3. Synthetic examples

3.1. Synthetic modelling

Synthetic modelling of IP responses was calculated using Res2dmod ver 3.01.93 (Loke, 2014). The software calculates the forward response in terms of apparent resistivity and apparent chargeability expressed as mV/V.

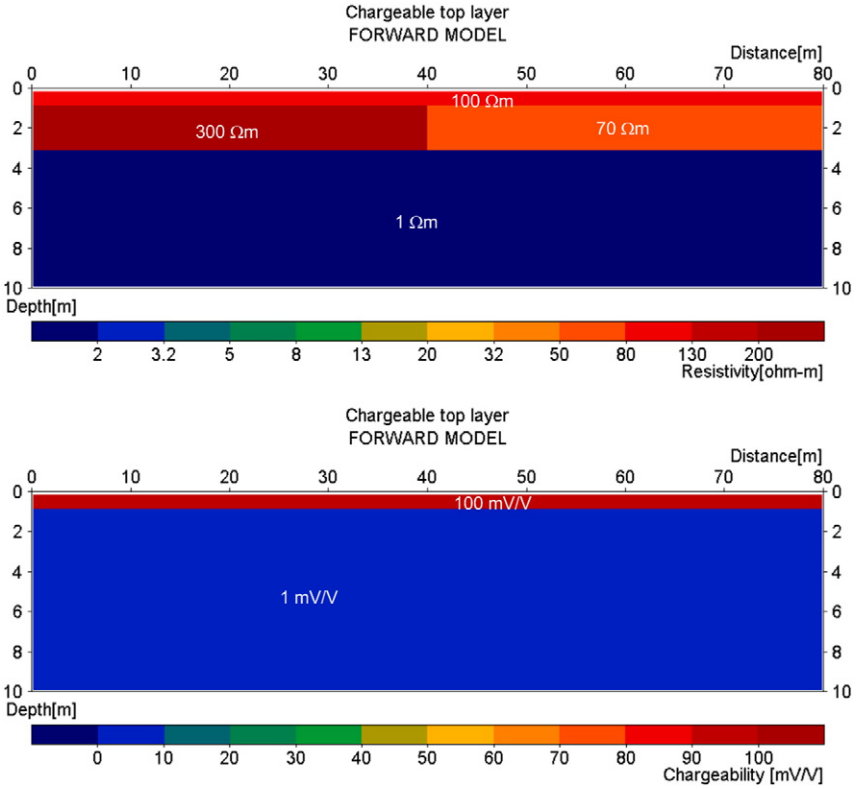

Fig. 3. Synthetic layer model with resistivity (upper) and chargeability (lower).

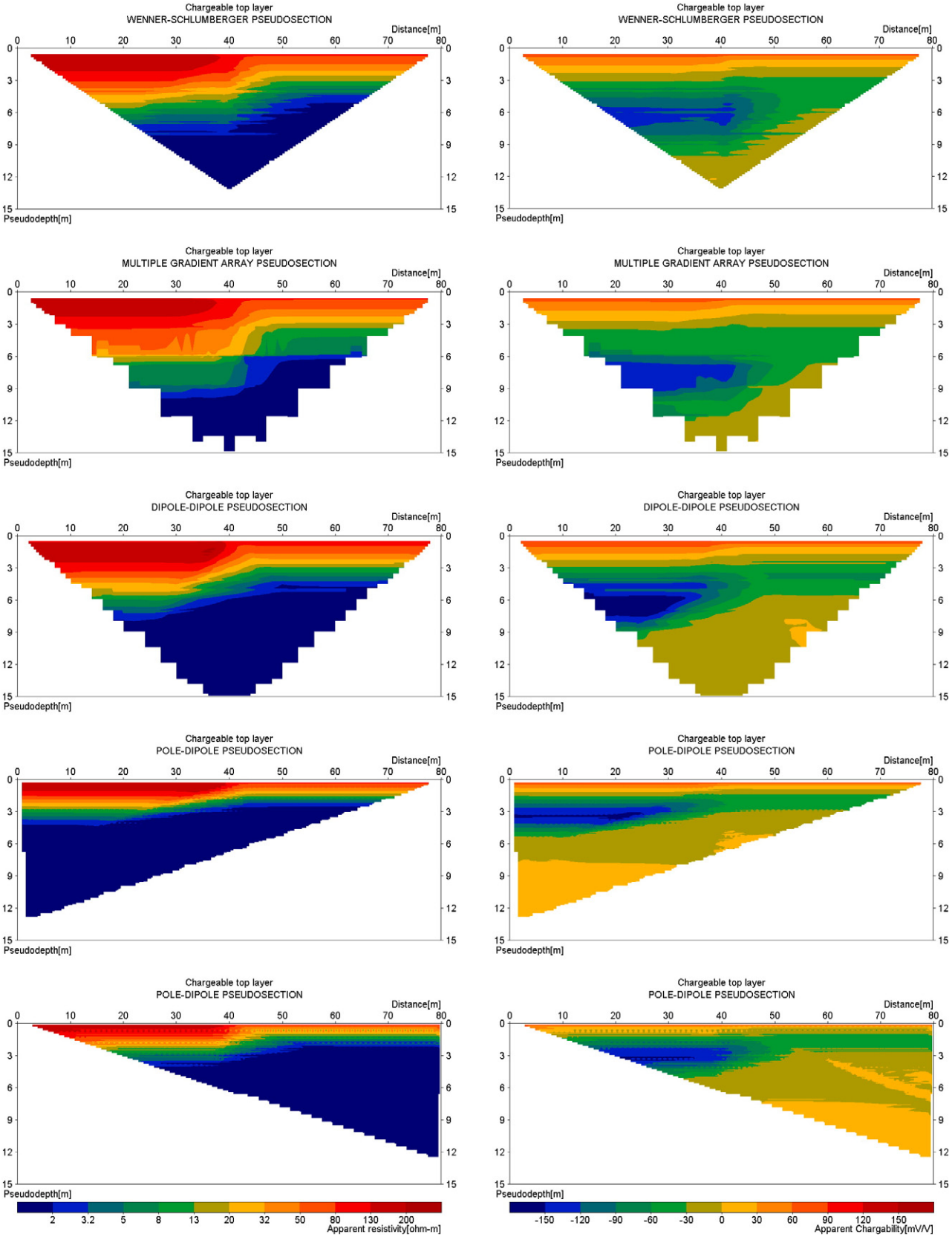

Fig. 4. Model responses for synthetic 3 layer model in Fig. 3. Apparent resistivity (left) and apparent chargeability (right) for from top to bottom; Wenner–Schlumberger, multiple gradient, dipole–dipole, forward pole–dipole and reverse pole–dipole array.

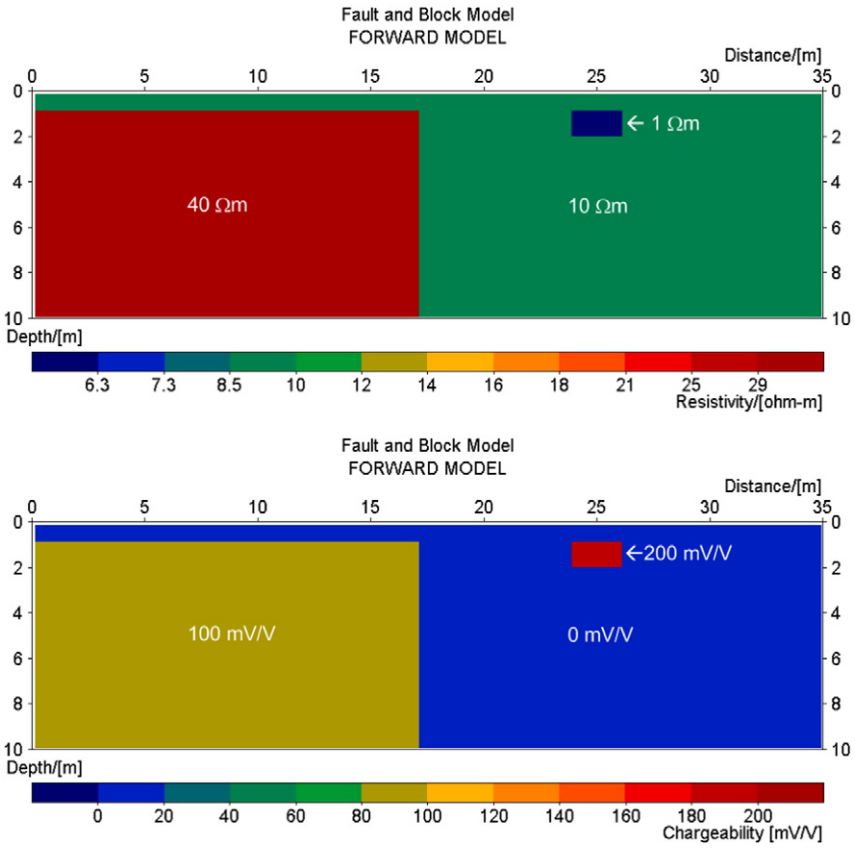

Fig. 5. Synthetic fault and block model with resistivity (upper) and chargeability (lower).

3.2. Chargeable top layer model

The model consists of three horizontal layers (Fig. 3); with a change in resistivity for the intermediate layer at the midpoint of the model. The resistivity from top to bottom is 100 Ωm, 300 Ωm and 1 Ωm in the left half, and 70 Ωm for the intermediate layer in the right half, with layer boundaries at 0.8 m and 3 m depth. The chargeability is essentially confined to the thin top layer with a chargeability of 100 mV/V, whereas the underlying layers are close to zero chargeability at 1 mV/V. The forward calculations were made for 81 electrodes with a separation of 1 m.

The model responses for layer model are plotted as pseudosections in Fig. 4, showing apparent resistivity and apparent chargeability for different electrode arrays (Wenner–Schlumberger, multiple gradient array, dipole–dipole, forward pole–dipole and reverse pole–dipole). All the resistivity pseudosections show a gradual decrease in apparent resistivity with increasing pseudodepth as could be expected, and the effect of the thin top layer is vaguely visible. There are distinct differences between the left and right half of the pseudosections as a result of the difference in resistivity of the second layer. The IP pseudosections exhibit positive apparent chargeability in the top couple of metres pseudodepth, under which negative values dominate. Maximum absolute magnitudes are visible at several metres pseudodepth, and it is notable that the absolute values of the negative apparent chargeabilities are larger than the chargeability of the forward model. The strongest negative values are found in the dipole–dipole array result which reach almost 200% absolute amplitude relative to the forward model. There are major differences in the magnitudes of the negative chargeabilities between the left and right half of the pseudosections, even though there is no lateral change in the chargeability of the layer in the synthetic model. This illustrates clearly that the apparent chargeability is not only dependent on the distribution of chargeability in the subsurface but that the resistivity distribution is also important.

3.3. Chargeable fault and block model

The second model consists of a block with 40 Ωm resistivity and 100 mV/V chargeability in the left half of the model (Fig. 5), overlain by a thin layer of 10 Ωm and 0 mV/V. The right half of the model has the same properties as the top layer, except for a low resistive (1 Ωm) and highly chargeable (200 mV/V) shallow block. The forward calculation was made for 35 electrodes with a separation of 1 m.

The model responses for the fault and block model are plotted as pseudosections in Fig. 6, showing apparent resistivity and apparent chargeability for different electrode arrays. The nested array (Wenner–Schlumberger and multiple gradient array) pseudosections have an appearance that rather well reflects the actual structure (Fig. 6 top, left), except that the low resistive anomaly bleeds down to large pseudodepths. The dipole–dipole and pole–dipole array exhibit large "panty leg" effects around the low resistive body (Fig. 6 mid and bottom, left). The IP pseudosections have a similar appearance with strong "panty leg" effects for the dipole–dipole and pole–dipole arrays (Fig. 6 mid and bottom, right), and these arrays also show many negative apparent chargeability data which is most prominent for dipole–dipole. The symmetrical nested Wenner–Schlumberger array does not have any negative IP data (Fig. 6 top, right), whereas the multiple gradient array section includes a few negative (Fig. 6 second from top, right) data points. This can be attributed to the different distribution of negative sensitivity zones for the latter, and how the chargeable zones are positioned in relation to these (Fig. 6).

4. Field example: data set recorded during field demo at IP workshop on Ile d'Oléron

4.1. Data acquisition

A demonstration of data acquisition with separated parallel cable spreads for current transmission and potential measurement (Dahlin

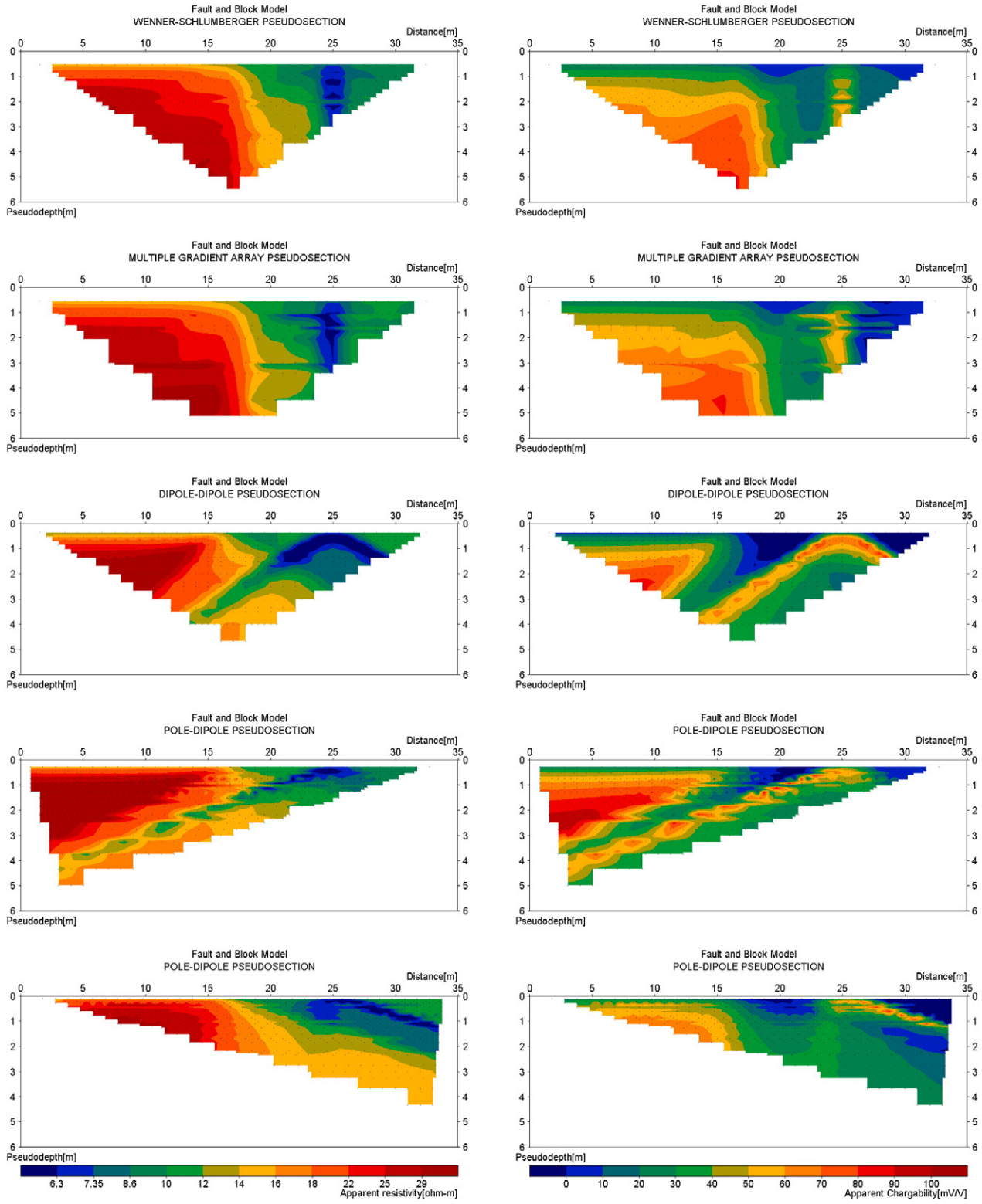

Fig. 6. Model responses for synthetic fault and block model in Fig. 5. Apparent resistivity (left) and apparent chargeability (right) for from top to bottom; Wenner–Schlumberger, multiple gradient, dipole–dipole, forward pole–dipole and reverse pole–dipole array.

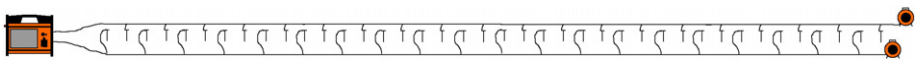

Fig. 7. Sketch of cable equipment setup used at field demo at 3rd IP workshop at Ile d'Oléron.

Fig. 8. Measurement demonstration in progress.

and Leroux, 2012) was made at the 3rd International Workshop on Induced Polarization held on Ile d'Oléron 7–9 April 2014. The site is geologically characterised by sedimentary deposits including marine clay, locally known as "bri", and river alluvium (Gouet, 2007).

The equipment used was an ABEM Terrameter LS with 8 measuring channels, two electrode cables with 32 take-outs each, 64 stainless steel electrodes and cable-to-electrode connectors. The instrument was powered by a 12 V DC battery. The electrodes were placed along a line with an electrode separation of 1 m. One electrode cable with take-out spacing 2 m was placed on each side of the electrode line and shifted 1 m relative to each other, so that every 2nd electrode was connected to respective cable (Fig. 7). The electrode cables were separated by a distance equivalent to twice the length of an electrode-to-cable jumper, i.e. around 1 m.

Fig. 8 shows the measurements in progress. The measurements were carried out while measurements with two other IP data acquisition were in progress nearby simultaneously, with associated current transmission. The current transmissions for these systems were done by an Iris Syscal Pro and a Radic Research HVPA600 respectively.

Multiple gradient array (Dahlin and Zhou, 2006) was used for the measurements, with a protocol comprising 1015 data points in total. Measuring was done with 1 s current-on and current-off time, and IP was measured in 8 time windows (20, 40, 60, 80, 120, 160, 200 and 280 ms long) starting 10 ms after current turn-off. Data stacking was limited to 2 repetitions per data point. The actual measurement of a complete data set took 37 min, excluding time to set up the system plus testing and improving electrode ground contact.

The electrode contact resistances were moderate with a mean value of 1.2 kΩ (Fig. 9). Transmitted current was in the range 85 to 500 mA, with a mean of 300 mA. There is a small variation in ground elevation along the line, which was not recorded due to lack of suitable equipment. The variation in contact resistance essentially reflects the variation in elevation, in that the ground was low lying and moist where the resistances are low and there is more relatively dry material above the wet horizon where the resistances are higher.

5. Field data results

The IP decay curves mostly have a simple decay shape, either positive or negative (see example in Fig. 10). In some cases the measured chargeabilities for the first time window (10–30 ms after current turn-off) are very high, maybe dependent on inductive coupling effects caused by the very high conductivity that are found at a few metres depth (see below). As a precaution the first time window was excluded when exporting data for inversion.

The resistivity pseudosection exhibits apparent resistivities ranging from less than 3 Ωm to above 100 Ωm (Fig. 11a), where the corresponding measured differential voltages range from less than 1 mV to around 7 V. The apparent chargeabilities are below 7 mV/V with negative values reaching tens of mV/V for the longest electrode separations (Fig. 11b). Since the chargeability is low many of the measured differential chargeability voltages are very small, ranging from below 1 μV to over hundred mV. There are 255 negative apparent chargeability data among the total 1015.

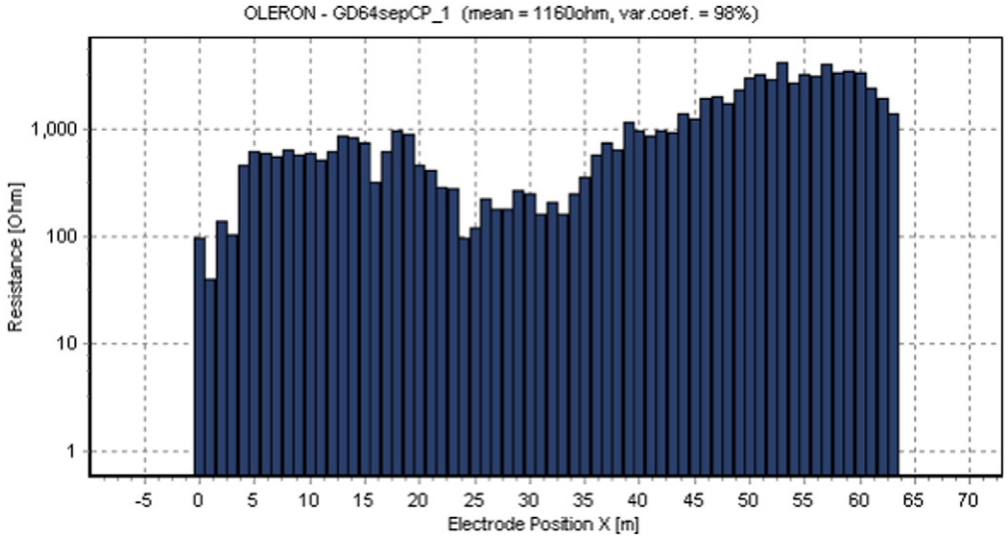

Fig. 9. Electrode contact resistances for field test at Ile d'Oléron.

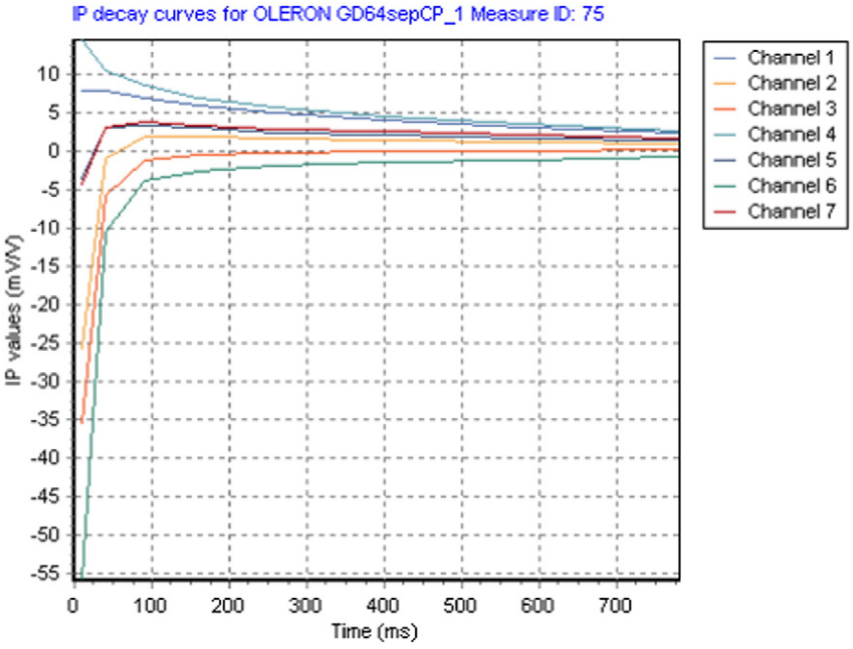

Fig. 10. Example of IP decay curves from field demo at 3rd IP workshop at Ile d'Oléron.

Due to noisy appearance of the IP data 14 out of the 1015 data points were removed before inversion. Considering that the measurements were made while other demonstrations with current transmission were in progress nearby for two other IP data acquisition systems this can be considered acceptable.

5.1. Inverted model sections

Inversion was carried out with RES2DINVx32 (ver. 3.71.96) using robust (L1 norm) inversion. So called model grid refinement was selected which means that there are two model cells between each electrode in the model instead of just one, which is generally necessary in order to achieve good model fit, and extended model was used. Furthermore vertical-to-horizontal flatness filter ration equal to 0.5 was used to optimise the model with regard to the expected predominantly horizontal character of the local geological environment. All other parameters were left at default settings. The inversion resulted in low mean residuals, 0.7% for the resistivity model and 1.4% for the chargeability model.

The resistivity model section (Fig. 12) shows two to three layers, where the upper 3–4 m thick layer can be interpreted as sandy sediments. The bottom layer is interpreted as the saline mud sediments of type "bri". The intermediate layer, or transition zone, increases in thickness in the rightmost part of the section where the model should be regarded with some caution because of poor data cover. This layer may be caused by sandy sediments with different water saturation compared to that above, or more fine grained sediments.

The inverted chargeability section (Fig. 12) shows a 1–2 m thick top layer with chargeability in the range of 4–8 mV/V, under which there is

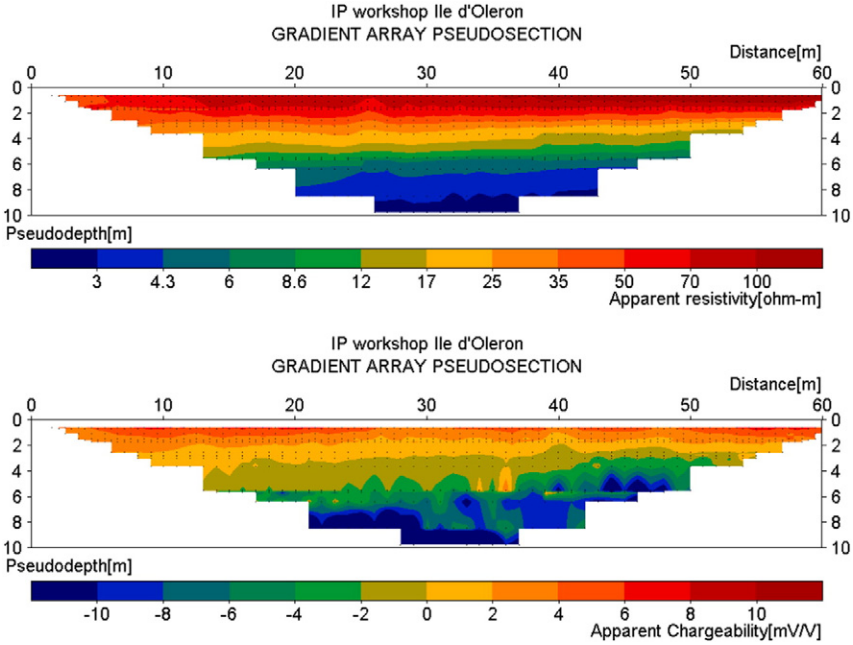

Fig. 11. Resistivity and chargeability pseudosection from field demo at 3rd IP workshop at Ile d'Oléron (integrated in the interval 30–940 ms).

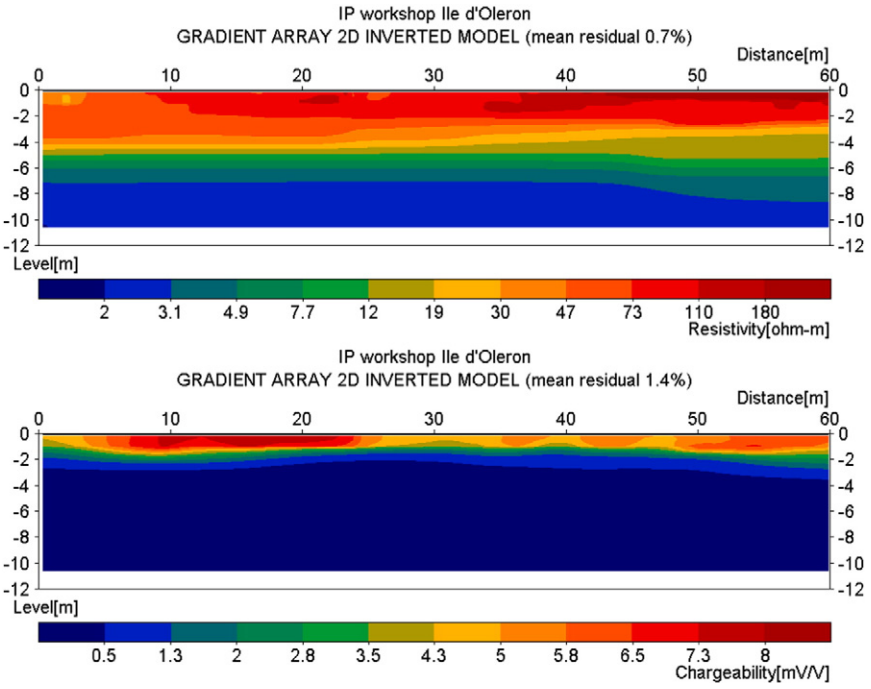

Fig. 12. Inverted resistivity and chargeability section based on data from field demo at 3rd IP workshop at Ile d'Oléron.

no detectable chargeability. The top layer can be interpreted as sandy sediments with organic content, below which there are sandy sediments followed by fine grained sediments. The lack of recorded IP response from the bottom layer shown by the resistivity section may be due to high salinity (Boadu and Seabrook, 2006; Weller et al., 2011).

A test was also made by removing all data points with negative apparent chargeability, and after editing away a few additional data with noisy appearance the number of data points were 757. Data were inverted using the same settings as the full data set which resulted in inverted sections with low residuals, 0.6% for both the resistivity and chargeability model (Fig. 13). Both model sections are, however, significantly different from the ones based on the original data set. The resistivity for the bottom layer is generally not as low, except for a low resistivity anomalous zone. The chargeability is very different with a high chargeability artefact at the bottom of the section, whereas the chargeability of the lower layer is otherwise low but not as low as the one for the original data set.

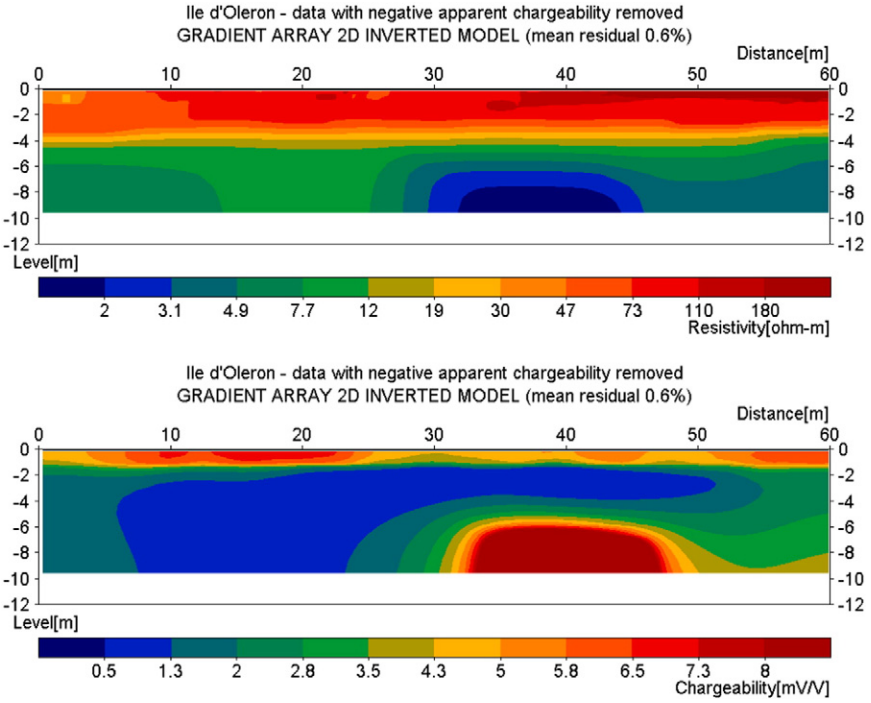

Fig. 13. Inverted resistivity and chargeability section based on data from field demo at 3rd IP workshop at Ile d'Oléron, where data points with negative apparent chargeability have been removed.

6. Discussion

The synthetic models clearly show that negative apparent chargeability can arise from the distribution of the chargeable zones. It typically happens when the chargeable material is restricted to a shallow layer, and the material below has little or no chargeability. The chargeable material will then to a large extent be concentrated in zones with negative sensitivity for longer electrode separations. This means that when transmitted current is turned off all contribution to the measured signal disappears immediately for the deeper parts where positive sensitivity dominates, whereas the chargeable near surface zones produce a potential that decays according to their IP properties. If the total signal contribution from areas with negative chargeability dominates it will result in negative apparent chargeability with IP decay curves that decay from negative towards zero. The sensitivity distribution for IP is a scaled version of that of resistivity (Oldenburg and Li, 1994), which means that the general pattern of positive and negative sensitivity zones is similar.

The synthetic examples show that the tendency to measure negative IP data differs between electrode arrays, where dipole–dipole produced most negative data and nested arrays least in the modelled examples. Pole-dipole array fell in between in this respect. Dipole-dipole array also gave the largest magnitude negative apparent chargeability, and it is notable that some of the modelled apparent chargeabilities have larger (negative) magnitude than the chargeability of the forward model.

IP decay IP curves recorded in the field can exhibit complex patterns that are not only a simple positive or negative decay, but appear to be a composite of decays. In is easy to imagine that complex distributions of chargeable material with different time constants distributed in zones of positive and negative sensitivity may create IP decay curves with composite shapes. In order to understand possible shapes of IP decay curves, in order to develop correct criteria for data editing routines, it is important to undertake numerical modelling of a suite of different resistivity and chargeability models. This is however beyond the scope of this paper.

The negative chargeabilities measured for the longer electrode spacings in the field example are in good accordance with the synthetic model results; they are a result of the chargeability distribution with a thin chargeable top layer overlying a layer with no detectable chargeability. The sensitivity distribution for longer electrode separations has major zones of negative sensitivity near the surface and positive sensitivity zones in the deeper parts (Fig. 12). The negative chargeabilities are enhanced by the resistivity distribution, with relatively high resistivity in the upper parts and very low resistivity at the bottom.

The inverted field example sections based on data set with negative apparent chargeability removed have poor definition of the lower parts and exhibit artefacts (Fig. 13). The reason for this is obviously that the majority of the data points for the largest electrode separations were removed, because those were the ones with negative apparent chargeability. This example clearly shows that removing the negative apparent chargeability data can seriously bias the inverted result.

The early times chargeabilites observed in the field data have much larger absolute magnitude than the chargeability of the top layer in the inverted model, which applies to positive as well as negative decays. Data for early time windows are of course always higher than for later time windows, meaning that data integrated over full decays are lower than from early time windows. The synthetic layer model example showed that integrated apparent chargeability can be larger than the chargeability of the forward model, and early times could be expected to have much higher magnitudes. This might offer an explanation for the very high magnitude early time IP data that is based on the sensitivity distribution rather than inductive effects, which would require more sophisticated IP modelling tools to investigate.

7. Conclusions

Negative data occur when the chargeable zones are predominantly located in zones of negative sensitivity. Apart from the relative position of the chargeable zones the resistivity distribution is important for the occurrence and magnitude of negative apparent chargeability, and situations where chargeable zones overly low resistive strata will generally produce negative IP data. These negative IP data contain essential information and exclusion of these means removing an important part of the information for the inversion. In addition intrinsic negative chargeability has been reported for soft clays, which further underlines that negative IP data should not be dismissed by default.

Acknowledgements

Funding for the work was provided by Formas—The Swedish Research Council for Environment, Agricultural Sciences and Spatial Planning (ref. 2012–1931), BeFo—Swedish Rock Engineering Research Foundation (ref. 331) and SBUF—The Development Fund of the Swedish Construction Industry (ref. 12719). The work was carried out within the Geoinfra-TRUST framework (http://trust-geoinfra.se/).

We wish to thank two anonymous reviewers and the editors for constructive criticism that improved the manuscript.

References

Auken, E., Pellerin, L., Christensen, N.B., Sørensen, K., 2006. A survey of current trends in near-surface electrical and electromagnetic methods. Geophysics 71 (5), G249–G260.
Bertin, B., 1976. Experimental and Theoretical Aspects of Induced Polarization, Vol. 1 Presentation and Application of the IP Method Case Histories. Gebrüder Borntraeger, Berlin 3 443 13009 7 (250 pp.).
Boadu, F.K., Seabrook, B.C., 2006. Effects of clay content and salinity on the spectral electrical response of soils. J. Eng. Environ. Geophys. 11 (3), 161–170.
Brandes, I., Acworth, R.I., 2003. Intrinsic Negative Chargeability of Soft Clays. Procs. ASEG 16th Geophysical Conference and Exhibition, February 2003, Adelaide.
Dahlin, T., 2001. The development of electrical imaging techniques. Comput. Geosci. 27 (9), 1019–1029.
Dahlin, T., Leroux, V., 2012. Improvement in time-domain induced polarisation data quality with multi-electrode systems by separating current and potential cables. Near Surf. Geophys. 10, 545–565.
Dahlin, T., Zhou, B., 2006. Multiple-gradient array measurements for multichannel 2D resistivity imaging. Near Surf. Geophys. 4, 113–123.
Dahlin, T., Rosqvist, H., Leroux, V., 2010. Resistivity-IP for landfill applications. First Break 28 (8), 101–105.
Dieter, K., Paterson, N.R., Grant, F.S., 1969. IP and resistivity type curves for three-dimensional bodies. Geophysics 34 (4), 615–632.
Fiandaca, G., Auken, E., Christiansen, A.V., Gazoty, A., 2012. Time-domain-induced polarization: full-decay forward modelling and 1D laterally constrained inversion of Cole–Cole parameters. Geophysics 77 (3), E213–E225.
Fiandaca, G., Ramm, J., Binley, A., Gazoty, A., Christiansen, A.V., Auken, E., 2013. Resolving spectral information from time domain induced polarization data through 2-D inversion. Geophys. J. Int. 192, 631–646.
Gazoty, A., Fiandaca, G., Pedersen, J., Auken, E., Christiansen, A.V., 2012. Mapping of landfills using time-domain spectral induced polarization data: the Eskelund case study. Near Surf. Geophys. 10, 575–586.
Gouet, O., 2007. Projet de classement au titre des articles L.341-1 et suivants du Code de l'Environnement De L'ÎLE D'OLÉRON, Report, Ministère de l'Écologie et du Developpement Durable. Département de la Charente-Maritime, Poitiers (84 pp.).
Hönig, M., Tezkan, B., 2007. 1D and 2D Cole–Cole-inversion of time domain induced-polarization data. Geophys. Prospect. 55, 117–133.
Jung, H.-K., Min, D.-J., Lee, H.S., Oh, S., Chung, H., 2009. Negative apparent resistivity in dipole–dipole electrical surveys. Explor. Geophys. 40, 33–40.
Leroux, V., Dahlin, T., Svensson, M., 2007. Dense resistivity and IP profiling for a landfill restoration project at Härlöv, Southern Sweden. Waste Manag. Res. 25 (1), 49–60.
Loeb, J., 1976. Experimental and Theoretical Aspects of Induced Polarization, Vol. 2 Macroscopic and Microscopic Theories. Gebrüder Borntraeger, Berlin 3 443 13010 0 (85 pp.).
Loke, M.H., 2014. Tutorial: 2-D and 3-D electrical imaging surveys, Revision date: 5th November 2014. www.geotomosoft.com (accessed 2015-02-19).
Loke, M.H., Chambers, J.E., Rucker, D.F., Kuras, O., Wilkinson, P.B., 2014. Recent developments in the direct-current geoelectrical imaging method. J. Appl. Geophys. 95, 135–156.
McGillivray, P.R., Oldenburg, D.W., 1990. Methods for calculating Fréchet derivatives and sensitivities for the non-linear inverse problem: a comparative study. Geophys. Prospect. 38, 499–524.
Nabighian, M.N., Elliot, C.L., 1976. Negative induced-polarization effects from layered media. Geophysics 41, 1236–1255.

Oldenburg, D.W., Li, Y., 1994. Inversion of induced polarization data. Geophysics 59, 1327–1341.
Ranieri, G., Ferrero, L., Godio, A., 1996. A geophysical study of a coastal plane in Sardinia. Ann. Geofis. XXXIX (1), 36–48.
Seigel, H.0., 1959. Mathematical formulation and type curves for induced polarization. Geophysics 24, 547–565.
Sumner, J.S., 1976. Principles of Induced Polarization for Geophysical Exploration. Elsevier 0444414819 (277 pp.).
Weller, A., Breede, K., Slater, L., Nordsiek, S., 2011. Effect of changing water salinity on complex conductivity spectra of sandstones. Geophysics 76 (5), F315–F327.